Dual-Arm Robotic Needle Insertion With Active Tissue Deformation for Autonomous Suturing

Fangxun Zhong, *Student Member, IEEE*, Yaqing Wang, Zerui Wang, *Member, IEEE*, and Yun-Hui Liu, *Fellow, IEEE*

***Abstract*—A major issue for needle insertion into soft tissue during suturing is the induced tissue deformation that hinders the minimization of tip-target positioning error. In this letter, we present a new robot control framework to solve target deviation by integrating active deformation control. We characterize the motion behavior of the desired target under needle-tissue interaction by introducing the needle-induced deformation matrix. Note that the modeling does not require the exact knowledge of tissue or needle insertion properties. The unknown parameters are online updated during the insertion procedure by an adaptive estimator via sensor-based measurement. A closed-loop controller is then proposed for dual-arm robotic execution upon image guidance. The dual-arm control aims to regulate a feature vector concerning the tip-target alignment to ensure target reachability. The feasibility of the proposed algorithm is studied via simulations and experiments on different biological tissues to simulate robotic minimally-invasive suturing using the da Vinci Research Kit as the control platform.**

***Index Terms*—Surgical robotics: laparoscopy, sensor-based control, medical robots and systems, dual arm manipulation.**

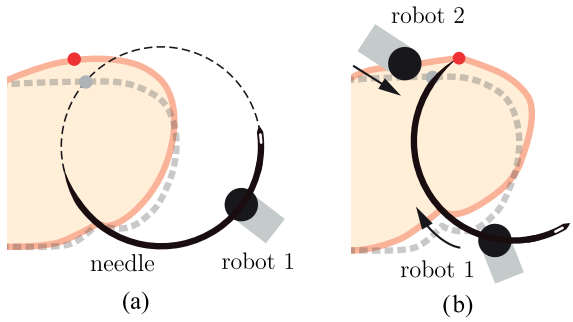

Fig. 1. (a) A 2D demonstration of tissue deformation induced by needle insertion (original shape shown as gray dash line) could remotely deviate the target (red dot) from its original position (gray dot). (b) Integrating active tissue control to needle insertion is expected to improve insertion accuracy, as adopted by manual suturing skills.

I. Introduction

NEEDLE insertion into soft tissue is a surgical procedure required by suturing for localized wound treatment. The primary goal is to guide the needle tip through the tissue towards a designated superficial target point, with the tip-target error (or the insertion error) being minimized [1]. Apart from precise needle handling, the compliant nature of tissue is a major issue which could lead to needle-induced deformation that remotely deviates the target from its original position [2]. In current clinical practice, needle insertion is collaborated by tissue manipulation from guidelines of suturing to reduce needle steering (a risk for tissue damage) [3], which is the primary motivation in this letter.

Robots have been clinically adopted to assist minimally-invasive surgeries [4]. Aiming for autonomous surgery, the robotic deformation regulation of soft tissue becomes of great significance to improve the suturing effectiveness. However, it imposes active manipulation of soft objects which remains a challenging topic in robot control [5]. During the insertion step, the needle tip continuously cracks the tissue body which involves complex needle-tissue interaction. The mechanical properties that characterize the local deformation behavior of tissue are crucial for robot control, but are usually unavailable in clinical applications. Introducing dual-arm robot manipulation strategy with weak dependence on mechanical modelling has the potential to automate minimally-invasive suturing with accurate and robust needle insertion (see Fig. 1 for conceptual description of our goal).

A. Related Work

Robotic control of needle insertion has been extensively studied [6]–[8]. Existing works have addressed individual problems of insertion force modelling [9], needle deflections [10], etc. Aiming for needle targeting, DiMaio *et al.* [6] proposed a position-based controller for placement of a straight needle via an MRI-compatible robot. Boctor *et al.* [11] developed an ultrasound-guided control algorithm for automatic needle insertion by means of virtual mechanical constraints. In [12] and [13], the needle was online navigated by visual servoing

Manuscript received January 10, 2019; accepted April 4, 2019. Date of publication April 24, 2019; date of current version May 8, 2019. This letter was recommended for publication by Associate Editor C. Bergeles and Editor P. Valdastri upon evaluation of the reviewers' comments. This work was supported in part by the HK RGC under T42-409/18-R, 14202918, and 415011, in part by the HK ITF under ITS/112/15FP and ITT/012/15GP, and in part by the project 4930745 of the CUHK T Stone Robotics Institute, CUHK. *(Corresponding author: Zerui Wang.)*

The authors are with the T Stone Robotics Institute and Department of Mechanical and Automation Engineering, The Chinese University of Hong Kong, Shatin, Hong Kong (e-mail: fxzhong@mae.cuhk.edu.hk; yaqingwang@cuhk.edu.hk; zrwang@mae.cuhk.edu.hk; yhliu@mae.cuhk.edu.hk).

This letter has supplementary downloadable material available at http://ieeexplore.ieee.org, provided by the authors. This video contains an animation showing the simulation results and footage displaying the experimental result of the case study. The total size of the file is 12 MB. Contact: Zerui Wang (zrwang@mae.cuhk.edu.hk) for further questions about this work.

Digital Object Identifier 10.1109/LRA.2019.2913082

control for suturing. Similar control methods were also adopted in [14]–[16] for needle-based procedures using CT or ultrasound guidance. Note that, the above works neglect the influence of tissue deformation on needle targeting results. On the other hand, many research groups focus on robotic control of flexible needles, for it exhibits greater steering performance for path planning in complicated tissue environment [17]–[20]. However, it is not preferred for suturing, where needle rigidity is still critical to generate enough interaction force for penetrating and cutting part of tissue.

Efforts have also been made to tackle tissue deformation to improve needle insertion accuracy. For example, in [21] and [22], it was discovered that needle insertion with tapping motion or faster insertion speed could reduce lateral motion or soft deformation of tissue. By using the finite element method (FEM), Alterovitz *et al.* [23] predicted tissue deformation with a biological model for inserting needle towards a sensorless target. Significant reduction of targeting error was reported via simulations. Kobayashi *et al.* [24] approached the procedure by applying tissue preloading to constant-velocity needle insertion. Smaller insertion error was reached by increasing the preloading force.

Active tissue deformation applied to precise needle insertion receives the least attention for its difficulty to obtain the exact modelling. Torabi *et al.* [25] presented a feedforward controller to manipulate tissue to correct needle insertion errors. A linear spring model was used to map the displacement relationship between the robot to the target. The ability for position correction of the target with obstacle avoidance was shown via simulations. In [26], a force-actuated position-controlled method was proposed to manipulate the tissue for needle targeting in breast biopsy. However, needle positioning was hard-coded with tissue being manipulated unidirectionally, which is deficient for solving target deviation in real cases. Meanwhile, our previous study in [27] used pure elastic model to solve soft object manipulation, which is impractical for needle insertion process where energy consumption appears during crack formation [28].

B. Contribution

This study is the first to implement adaptive control scheme to tissue deformation regulation during needle insertion. To achieve "targeting under deformation", we first propose a new deformation modelling under needle-tissue interaction without knowing the exact parameters of tissue deformation properties and needle insertion mechanics. Those parameters are adaptively estimated via sensor-based measurements to refine the motion behavior between the target and needle/tissue manipulators. We further develop a dual-arm controller to simultaneously regulate the tissue deformation and needle tip position. The stability of the control framework is guaranteed to robustly deal with inaccurate robot-camera calibration and small perturbation, whose feasibility and performance is further evaluated via simulations and experiments.

The letter is structured as follows: Section II states the basic models and assumptions adopted to our method. Sections III and IV give our deformation modelling and controller design. Section V presents the results of the study. Conclusions and future works are given in Section VI.

II. Preliminaries

A. Needle Insertion Modelling

Deformation of soft tissue (originally static and undeformed) during needle insertion is attributed to needle-tissue interaction force (denoted by f_n). It has been widely accepted that the value consists of the following independent terms [29]:

$$f_n = f_c + f_f + f_s \tag{1}$$

where the stiffness force f_s refers to the load between the needle tip and tissue surface at pre-puncture phase, which becomes negligible during the (quasi-static) insertion phase after a crack is formed on tissue [29]. The frictional force f_f is mainly generated on the side of the needle body. To reach a larger insertion depth of the needle tip, cutting force f_c is critical for tissue crack growth along tip direction, which is ideally constant for a given needle and (homogeneous) tissue [9], [29]. This facilitates access to investigation of needle-induced tissue deformation behavior, which is important for robot-controlled targeting of soft objects.

Biological tissues exhibit linear elasticity subject to local deformations [30]. Assuming an instant moving distance δl of needle tip along its tangent direction, there exists the following relationship [28]:

$$\delta W_N = \delta W_R + \delta \Lambda + f_f(l)\delta l \tag{2}$$

where the work $\delta W_N = f_n \delta l$ done by the needle is initially transferred to (elastic) potential energy $\delta\Lambda$ stored in the tissue, which increases the needle-tissue contact force and cracks the tissue body when the value surpasses f_c. Under quasi-static modelling that the needle inserts "slowly", $\delta\Lambda$ is sufficiently released while the contact force remains f_c, i.e., the work done by the needle insertion is irreversibly consumed for crack propagation inside tissue [31], denoted by δW_R. The frictional force $f_f(l)$ upon "slow" insertion is assumed to exert subtle influence on the local deformation around the needle tip [28], leading (2) to be simplified to $\delta W_N \approx \delta W_R$.

B. Problem Formulation

We focus our attention of needle insertion on minimally-invasive suturing, where the user-defined target is a single superficial point on tissue in each suturing throw, which is to be penetrated by the needle tip from underneath. Two robot arms provide rigid grasping of the needle and tissue without slippage. The needle's pose relative to the corresponding end-effector is invariant during stitching, which is initially absent in the system.[1] The position of the target is constantly localized via sensor-based measurements to provide feedback input for the procedure, while the needle experiences partial occlusion after the insertion begins. Unlike many existing approaches, we generalize the problem by considering a weakly-fixed tissue that the target is easily deviated

[1]This statement is made by neglecting the needle deflection during insertion, since suturing needles are usually significantly stiffer than tissues.

in 3D Cartesian space, which is more common in practice. To satisfy the above needle insertion modelling using quasi-static manipulation, the robot arms are suggested to move smoothly and slowly (by regulating their maximum motion speeds), which is reasonable when performing such a delicate task. The exact mechanical properties of tissue and needle insertion are unknown and will be online estimated. The task effectiveness is primarily evaluated by the evolution of the final (minimized) value of the tip-target distance.

III. Deformation Modelling

Consider a biological tissue undergoing linear elastic deformation subject to both needle insertion and robot manipulation. Denote the robot grasping point on the tissue and the needle tip position by $\mathbf{x}_m$, $\mathbf{x}_n \in \mathbb{R}^3$ in 3D Cartesian space, respectively. Given the assumption in Section II that the procedure satisfies quasi-static process, the internal forces (from elastic deformation) and external forces (led by robot-actuated manipulation) are always balanced. Thus, the (elastic) potential energy U in the system dominates the kinetic energy with negligible inertial effects. Based on the above statements, we give the following equilibrium equation:

$$\frac{\partial U}{\partial \mathbf{p}}^{\intercal} = \mathbf{0}_{3\times 1} \tag{3}$$

where $\mathbf{p}$ denotes the target position to be reached by the needle tip. The remaining non-target points on the tissue are considered distant from the robot-manipulated points $\mathbf{x}_m$ and $\mathbf{x}_n$, hence their influence on the local deformation behavior is negligible compared to robot manipulation [27]. Implementing first-order Taylor expansion of (3) around the equilibrium reveals a linearized displacement relationship between robot target deviation and robot-actuated motions as follows:

$$\underbrace{\frac{\partial^2 U}{\partial \mathbf{p}\partial \mathbf{p}}}_{\mathbf{A}}\delta\mathbf{p} + \underbrace{\frac{\partial^2 U}{\partial \mathbf{x}_m\partial \mathbf{p}}}_{\mathbf{B}}\delta\mathbf{x}_m + \underbrace{\frac{\partial^2 U}{\partial \mathbf{x}_n\partial \mathbf{p}}}_{\mathbf{C}}\delta\mathbf{x}_n = 0 \tag{4}$$

where $\delta\mathbf{p} = \mathbf{p} - \mathbf{p}^*$, $\delta\mathbf{x}_m = \mathbf{x}_m - \mathbf{x}_m^*$ and $\delta\mathbf{x}_n = \mathbf{x}_n - \mathbf{x}_n^*$ define the infinitesimal displacements of the interested points from the equilibrium state. To study the role of local tissue deformation in relationship (4), we give the linear elastic force generated inside the tissue body:

$$\mathbf{f}_e(\mathbf{v}) = -\nabla_{\mathbf{x}} U = k(||\mathbf{v}|| - l)\mathbf{v}/||\mathbf{v}|| \tag{5}$$

where $\mathbf{v} \in \mathbb{R}^3$ denotes the considered force direction; the unchanged properties k and l suggest the tissue is homogeneous under either compressing or stretching. Similar to (3), an equation can be derived in terms of $\mathbf{x}_n$ as

$$\frac{\partial U}{\partial \mathbf{x}_n}^{\intercal} - \mathbf{f}_n = \mathbf{0}_{3\times 1} \tag{6}$$

where $\mathbf{f}_n = f_c\mathbf{t}_n/||\mathbf{t}_n|| \in \mathbb{R}^3$ is the cutting force along the (measurable) tip's tangent direction $\mathbf{t}_n \in \mathbb{R}^3$. The resultant load applied to the tissue body, transmitted via elastic deformation, further affects the position of the target remotely. By combining (5) and (6), the total force applied to the target owns the following independent terms:

$$\frac{\partial U}{\partial \mathbf{p}}^{\intercal} = \zeta(\mathbf{p}, \mathbf{x}_m) + \eta(\mathbf{p}, \mathbf{x}_n, \mathbf{t}_n) \tag{7}$$

where $\zeta(\cdot)$ and $\eta(\cdot)$ denote the conservative force and the needle-induced elastic load from the cutting force $\mathbf{f}_n$ along the unit vector $\mathbf{v}_2 = (\mathbf{p} - \mathbf{x}_n)/||\mathbf{p} - \mathbf{x}_n||$, respectively. Here, we denote the elastic load that explicitly relies on f_c:

$$\eta(\mathbf{p}, \mathbf{x}_n) = f_c g(\mathbf{p}, \mathbf{x}_n, \mathbf{t}_n) \tag{8}$$

where $g(\cdot)$ relates to the stress field distributed towards the tissue whose form is determined when fracturing an elastic body [32]. Introducing (5) and (8) to (7) yields

$$\begin{aligned}\mathbf{A} &= \frac{\partial}{\partial \mathbf{p}}\zeta(\cdot) + \frac{\partial}{\partial \mathbf{p}}\eta(\cdot) \\ &= \mathbf{K}_A(\mathbf{p}, \mathbf{x}_m, \mathbf{x}_n, \mathbf{t}_n)\underbrace{\begin{bmatrix} k\mathbf{I}_3 & kl\mathbf{I}_3 & f_c\mathbf{I}_3 \end{bmatrix}^{\intercal}}_{\mathbf{\Theta_A}}\end{aligned} \tag{9}$$

where $\mathbf{K}_A(\cdot) \in \mathbb{R}^{3\times 9}$ is the stiffness matrix with $\mathbf{I}_3 \in \mathbb{R}^{3\times 3}$ being the identity matrix. Note that the unknown parameters and the computable data ($\mathbf{p}, \mathbf{x}_m$ and $\mathbf{x}_n$) have been organized separately via factorization of matrix $\mathbf{A} \in \mathbb{R}^{3\times 3}$. Meanwhile, we derive the following equations

$$\frac{\partial}{\partial \mathbf{x}_m}\zeta(\cdot) = \mathbf{K}_B(\mathbf{p}, \mathbf{x}_m)\underbrace{\begin{bmatrix} k\mathbf{I}_3 & kl\mathbf{I}_3 \end{bmatrix}^{\intercal}}_{\mathbf{\Theta_B}}, \tag{10a}$$

$$\frac{\partial}{\partial \mathbf{x}_n}\eta(\cdot) = f_c\mathbf{K}_C(\mathbf{p}, \mathbf{x}_n, \mathbf{t}_n)\mathbf{I}_3. \tag{10b}$$

Substituting (9)–(10) into (4) yields

$$\delta\mathbf{p} = \mathbf{D}\begin{bmatrix} \delta\mathbf{x}_m & \delta\mathbf{x}_n \end{bmatrix}^{\intercal} \tag{11}$$

which characterizes a linearized displacement mapping from the target $\delta\mathbf{p}$ to dual-arm robot actuations $\delta\mathbf{x}_m$ and $\delta\mathbf{x}_n$. We name the matrix $\mathbf{D} \in \mathbb{R}^{3\times 6}$ as *needle-induced deformation matrix* whose detailed form is presented by

$$\mathbf{D} = \begin{bmatrix} -\mathbf{\Theta}_A^+\mathbf{K}_A^+\mathbf{K}_B\mathbf{\Theta}_B & -f_c\mathbf{\Theta}_A^+\mathbf{K}_A^+\mathbf{K}_C \end{bmatrix} \tag{12}$$

where the factored form $\mathbf{A}^+ = \mathbf{\Theta}_A^+\mathbf{K}_A^+$ is the pseudoinverse. As a result, the elements of the matrix $\mathbf{D}$ share the following identical form:

$$\big[\mathbf{D}\big]_{i,j} = \sum_{r=1}^{3\times 6} w_{i,j} \cdot a_{i,j} \tag{13}$$

where the scalar $w_{i,j}$ and $a_{i,j}$ imply the knowledge of computable data and unknown parameters, respectively. The illustrated modelling diagram is shown in Fig. 2. Up to now, a characterization of the tissue's deformation behavior subject to needle insertion and tissue manipulation has been obtained, which is useful for designing the dual-arm controller to be introduced in the next section.

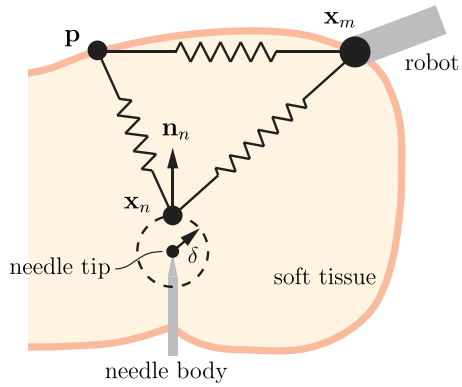

Fig. 2. Conceptual demonstration of deformation modelling considering needle insertion and robot manipulation.

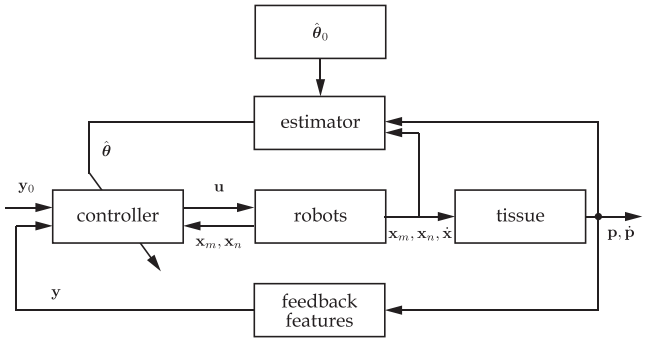

Fig. 3. The control diagram of our dual-arm control strategy, where the needle motion is depicted by the robot actuation input for tissue control.

IV. Controller Design

A. Adaptive Estimator

To utilize the local deformation behavior such that the target point motion can be controlled by robot manipulation, the unknown parameters appear (11) should be online estimated by the system. The overall design of our controller can be referred to Fig. 3. We start by computing the velocity mapping between the target to robot end-effectors as follows:

$$\dot{\mathbf{p}} = \underbrace{\mathbf{D}\begin{bmatrix} \mathbf{R}_m & \mathbf{0} \\ \mathbf{0} & \mathbf{R}_t\mathbf{R}_n \end{bmatrix}}_{\overline{\mathbf{D}}} \begin{bmatrix} {}^{b_m}\dot{\mathbf{x}}_m \\ {}^{b_n}\dot{\mathbf{x}}_n \end{bmatrix} \tag{14}$$

where $\mathbf{R}_m$ and $\mathbf{R}_n$ describe the constant orientations to transform the motion from the camera to robot base, denoted by ${}^{b_m}\dot{\mathbf{x}}_m$ and ${}^{b_n}\dot{\mathbf{x}}_n$, respectively. The matrix $\mathbf{R}_t$ depicts the tool-tip rotation, which is invariant and computable prior to the control phase via image-based input. Based on the relationship in (14), the unknown needle-tissue interaction properties can be linearly parameterized to the following:

$$\dot{\mathbf{p}} = \mathbf{W}(\mathbf{x}_m, \mathbf{x}_n, {}^{b_m}\dot{\mathbf{x}}_m, {}^{b_n}\dot{\mathbf{x}}_n)\boldsymbol{\theta} \tag{15}$$

where $\mathbf{W}(\cdot) \in \mathbb{R}^{3\times l}$ is the linear regression matrix. The column vector $\boldsymbol{\theta} \in \mathbb{R}^l$ relates to the unknown parameters including from the needle-tissue cutting force, the elastic properties of tissue, and robot-camera calibration. An imperfect model of $\hat{\boldsymbol{\theta}}$ will lead to the following motion flow error

$$\Delta\mathbf{p} = \dot{\mathbf{p}} - \hat{\dot{\mathbf{p}}} = \mathbf{W}\Delta\boldsymbol{\theta} \tag{16}$$

where $\Delta\mathbf{p}$ describes the motion error attributed to the discrepancy of deformation model between the estimation ($\hat{\dot{\mathbf{p}}} = \mathbf{W}\hat{\boldsymbol{\theta}}$) and its true one, i.e., $\Delta\boldsymbol{\theta} = \boldsymbol{\theta} - \hat{\boldsymbol{\theta}}$. To deal with this error, we introduce a quadratic cost function defined by

$$V = \frac{1}{2}\Delta\mathbf{p}^\intercal\Delta\mathbf{p}. \tag{17}$$

We then update the parameters online by implementing the gradient descent rule

$$\frac{d}{dt}\hat{\boldsymbol{\theta}} = -\boldsymbol{\Gamma}\frac{\partial V}{\partial\hat{\boldsymbol{\theta}}}^\intercal \tag{18}$$

where $\boldsymbol{\Gamma}$ is the positive-definite gain matrix. The updating scheme corrects the model $\hat{\boldsymbol{\theta}}$ via continuously inspecting the measured motion flow $\dot{\mathbf{p}}$. This is a central step in our modelling to "learn" the non-rigid motion behavior while commanding the robot arms to complete needle targeting.

Remark 1: The final estimate of the parameters in $\boldsymbol{\theta}$ may not reach their true values since their dimension is larger than that of the output ($l > 3$). However, we point out that our ultimate goal is to minimize the tip-target error instead of accurate model identification, with the stability of the closed-loop system still being guaranteed by our controller.

Remark 2: The adaptive updating law can deal with coarse computation of $\mathbf{R}_m$, $\mathbf{R}_n$, and $\mathbf{R}_t$ subject to inaccurate robot-camera calibration and sensor measurement.

B. Robot Controller

A feedback controller is designed in this subsection to ensure minimization of the needle insertion error. We summarize the robot-controlled motions with respect to their base frame by a new unified vector described by

$$\dot{\mathbf{x}} = \begin{bmatrix} {}^{b_m}\dot{\mathbf{x}}_m & {}^{b_n}\dot{\mathbf{x}}_n \end{bmatrix}^\intercal. \tag{19}$$

Define a linearly-independent feedback feature vector $\mathbf{y}(\mathbf{p})$ which characterizes our control objective using the target position. Then, one can compute the time derivative of (19) by

$$\dot{\mathbf{y}}(t) = \underbrace{\frac{\partial\mathbf{y}}{\partial\mathbf{p}}(\mathbf{p}(t))\frac{\partial\mathbf{p}}{\partial\mathbf{x}}(\mathbf{x}(t))}_{\mathbf{J}}\dot{\mathbf{x}}(t) \tag{20}$$

where $\mathbf{y} \in \mathbb{R}^2$ denotes the designated feedback feature vector. The total feature-to-robot interaction matrix $\mathbf{J} \in \mathbb{R}^{2\times 6}$ can be further expressed as follows

$$\mathbf{J} = \frac{\partial\mathbf{y}}{\partial\mathbf{p}}(\mathbf{p})\overline{\mathbf{D}}. \tag{21}$$

The matrix $\partial\mathbf{y}/\partial\mathbf{p}$ can be determined by a given form of $\mathbf{y}(\mathbf{p})$. We propose the following feedback control law towards robot manipulations:

$$\mathbf{u} = -\hat{\mathbf{J}}^{+}\mathbf{K}\frac{\partial}{\partial\mathbf{y}}Q(\mathbf{y}) \tag{22}$$

where the matrix $\hat{\mathbf{J}}^{+} \in \mathbb{R}^{6\times 2}$ denotes the Mooore-Penrose inverse matrix constructed by the estimated parameters $\hat{\boldsymbol{\theta}}$. Thus,

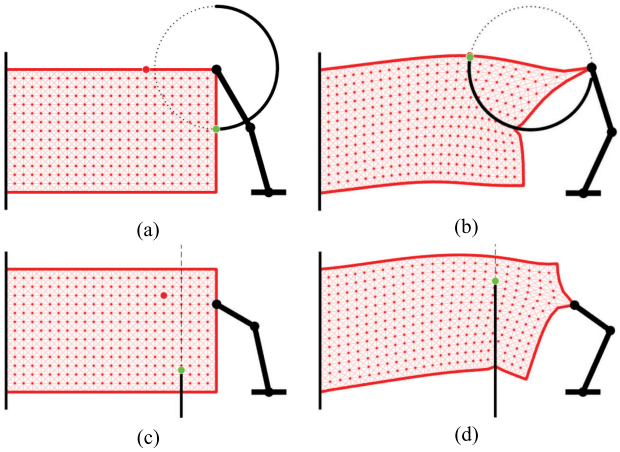

Fig. 4. Simulation results of dual-arm needle insertion into soft tissue using circular and straight needle respectively (the target marked in red and the tip marked in green).[2]

given the control input $\mathbf{u}(t) = \dot{\mathbf{x}}(t)$, the robot-actuated motions are controlled by a pre-set gain matrix $\mathbf{K} \in \mathbb{R}^{2\times 2}$. The scalar Q is a quadratic cost function with

$$Q = \frac{1}{2}||\mathbf{y}(\mathbf{p})||^2 \tag{23}$$

which can be used to minimize the feedback features in $\mathbf{y}$ if the desired $\mathbf{y}_d$ is nothing but $\mathbf{0}_{2\times 1}$.

Proof: Substituting (22) and (23) back to (20) using the estimated interaction matrix $\dot{\mathbf{y}} = \hat{\mathbf{J}}\dot{\mathbf{x}}$ will lead to the following closed-loop system:

$$\dot{\mathbf{y}} = -\mathbf{K}\mathbf{y} \tag{24}$$

which yields a linear stable system that the elements in vector $\mathbf{y}$ asymptotically converge to zeros regulated by $\mathbf{K}$. ■

C. Feedback Feature Vector

Manipulating the needle tip towards the target can be achieved by infinite solutions of tip trajectories. However, this must be further constrained to ensure the following: 1) the needle tip does not miss the target and/or experiences back dragging; 2) the target keeps away from the lateral side of the needle, where needle-induced tissue heterogeneity makes the target harder to be manipulated. We deal with these cases by introducing a parallel control objective as "target alignment", i.e., to land the target on the expected needle insertion trajectory ahead of the tip, which is further interpreted by the following feedback feature vector

$$\mathbf{y} = \begin{bmatrix} ||\mathbf{p} - \mathbf{x}_n|| & y_s \end{bmatrix}^\intercal \tag{25}$$

where y_s denotes the secondary control objective apart from the targeting error. For circular needle used in minimally-invasive suturing, the virtual feature y_s is defined by

$$d = ||\mathbf{p} - \mathbf{x}_n|| - r_n \tag{26}$$

[2]We omit the the needle manipulator to avoid visual clutter in illustration.

where r_n refers to the radius of the circle along needle body. Thus, the target is preferentially moved to the circular trajectory to be followed by the needle with $y_s = d$. For generality, we also give the feedback feature while using a straight rigid needle for needle based procedures

$$\alpha = arcsin\left(\frac{(\mathbf{p} - \mathbf{x}_n) \times \mathbf{t}_n}{||\mathbf{p} - \mathbf{x}_n||||\mathbf{t}_n||||\mathbf{n}_n||}\right) \tag{27}$$

where $y_s = \alpha$ gives the angle of deviation and $\mathbf{n}_n$ is the normal vector computed from the cross product. Here note that the selected $\mathbf{y}$ enables the target to land on the tip trajectory accompanied by targeting error minimization. The norm of the tip-target positioning error $||\mathbf{p} - \mathbf{x}_n||$ enforces the controller response to rely on the total tip-target distance.

V. Results

A. Simulation I: Feasibility Study

We construct a virtual planar soft tissue which exhibits two-dimensional deformation in our simulations. We use the finite element method (FEM) with displacement-based input to update its deformation behavior subject to kinematic robot control. There are 25×15 nodes forming a rectangular tissue shape, with each in-between connection depicts a linear elastic truss with 3 pixels (pxs) in length to simulate tissue homogeneity, whose exact mechanical properties are identical but unknown to the controller. The tissue experiences constant cutting force at the needle tip. Nodes located along the side wall of the needle encounter frictional force whose model is referred to the modelling in [8]. The tissue and needle manipulators are 2-degree-of-freedom (2-DoF) planar robots with known kinematics. The simulation is conducted via MATLAB R2017a by MathWorks, Inc.

Two groups of simulations are conducted. One uses a 1/2 circular needle to reach a superficial target point from underneath the tissue as in laparoscopic suturing, with the other using a straight needle with a subsurface target to simulate straight needle insertion. We further constrain the motion velocities of the needle manipulator such that

$$\bar{\dot{\mathbf{x}}}_\mathbf{n} = \begin{cases} \frac{\dot{\mathbf{x}}_n \cdot \mathbf{t}_n}{||\dot{\mathbf{x}}_n||||\mathbf{t}_n||}\mathbf{t}_n & ||\mathbf{p} - \mathbf{x}_n|| > \epsilon \\ 0 & ||\mathbf{p} - \mathbf{x}_n|| < \epsilon \end{cases} \tag{28}$$

where the constant scalar ϵ is a pre-set small Euclidean distance (0.1 px) that ends the control process. This allows the needle tip to move along its tangent direction to minimize the shear deformation of tissue. In both cases, the controller is implemented with $\mathbf{K} = diag(0.01, 0.25)$, with the norm of step motions $\dot{\mathbf{x}}_m$ and $\dot{\mathbf{x}}_n$ being saturated to 0.1 px. Targets are both away from the needle tip (> 25 pxs) and are misaligned with the tip trajectory at $t = 0$. The evolution of the commanded motions to the tissue and needle manipulators are shown in Fig. 5 as $||\dot{\mathbf{x}}_m||$ and $||\dot{\mathbf{x}}_n||$, respectively, from which the needle insertion speed increases as the tissue manipulation stabilizes after target alignment. The tissue manipulator continuously moves the tissue to compensate target deviation caused by deformation. Fig. 4 illustrates the control results of the two scenarios at their initial ((a) and (c)) and final configurations ((b) and (d)), respectively,

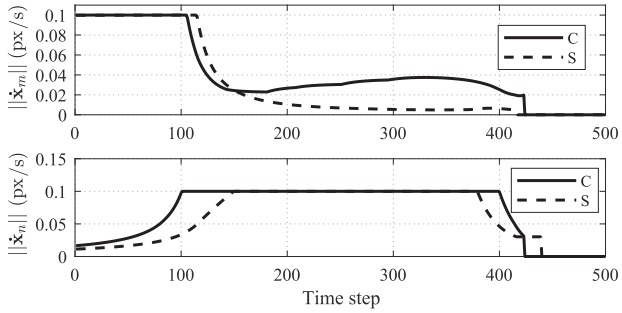

Fig. 5. Robot-actuated motion velocities ($\dot{\mathbf{x}}_m$ for tissue manipulator and $\dot{\mathbf{x}}_n$ for needle manipulator) subject to saturated magnitudes (C means the case with circular needle, S for straight needle).

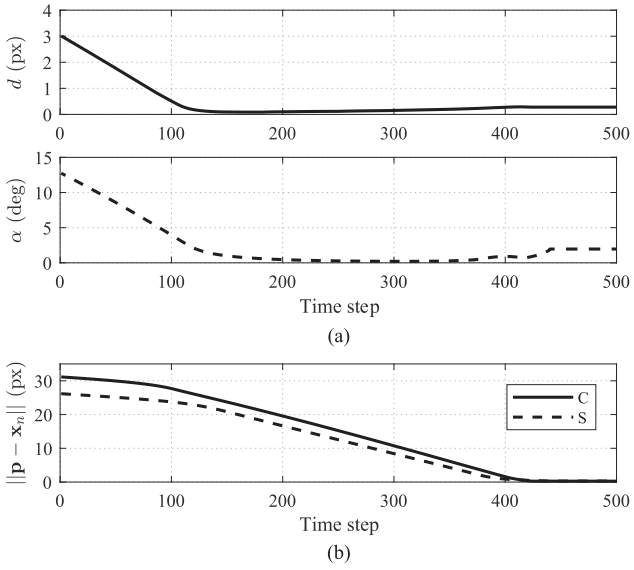

Fig. 6. (a) Evolution of the feedback features during needle insertion control (d with circular needle and α with straight needle). (b) Evolution of the tip-target distance (C for circular needle, S for straight needle).

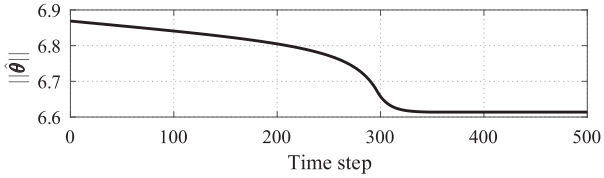

Fig. 7. The convergence of the estimated parameters in the case of circular needle insertion, depicted by $||\hat{\boldsymbol{\theta}}||$ as time elapses.

where the tissue manipulation point, the target and the initial needle position are congfigured differently. The virtual features d and α are minimized for target alignment as shown in Fig. 6(b), followed by the targeting errors converging to zeros at later time steps in Fig. 6(a). The slight deviation of d and α from 0 as the needle tip approaches the target is attributed to the change of the tip-target motion mapping to be estimated by the controller under a constant $\mathbf{K}$. Fig. 7 further shows the settlement of estimated parameters as time elapses for circular needle insertion, from which we depict the convergence via $||\hat{\boldsymbol{\theta}}||$ due to the large dimension of $\hat{\boldsymbol{\theta}}$. Note that this does not necessarily imply that

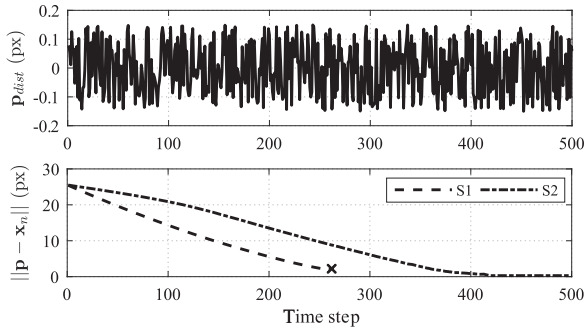

Fig. 8. The added random noise to S3 (above) and the targeting errors in three control configurations (below). The marked "x" in the graph is the time step when the error is minimized in S1.

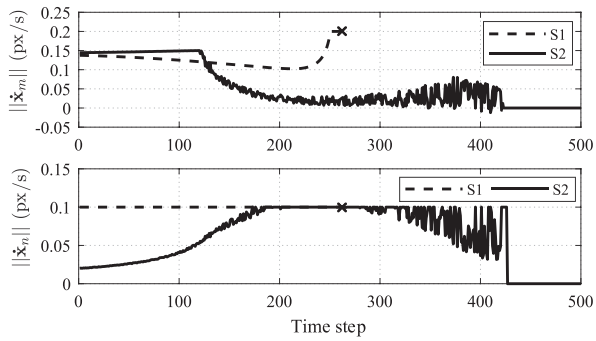

Fig. 9. Motion speed values commanded to the tissue and needle manipulator respectively, which become 0 s after the targeting errors become smaller than the preset ϵ.

the parameters have reached their true values, but contributes to the stable minimization of the final insertion error.

B. Simulation II: Comparative Study

We further conduct a comparative study to demonstrate the effectiveness of our control scheme. We consider straight needle insertion (whose performance similar to the local behavior for a circular needle) with the virtual tissue model identical as in Section V-B.[3] Two control configurations are tested: 1) open-loop needle insertion with active tissue control (S1); and 2) dual-arm needle and tissue control with disturbance (S2). We define the initial condition that $\alpha = 20^\circ$, with the saturated norms of robot motions $\dot{\mathbf{x}}_m$ and $\dot{\mathbf{x}}_n$ set to 0.15 px and 0.1 px per step, respectively. A random noise with uniform distribution ($\pm$0.15 px) is added to $\mathbf{p}$ to reappear the rough sensor-based measurement in real cases. The targeting results are graphed in Fig. 8. In S1, the needle tip misses the target (targeting error 1.9 pxs) due to open-loop insertion control. By contrast, the dual-arm control in S2 minimizes the insertion error smoothly ($<$0.1 px as set by ϵ) regardless of perturbations. The needle insertion speed is regulated as the target approaches the tip trajectory. The motions from both manipulators are settled compared to that of S1 (Fig. 9).

[3]While needle deflection is common for straight needles, we conduct such simulation to show the controller feasibility under different set-ups.

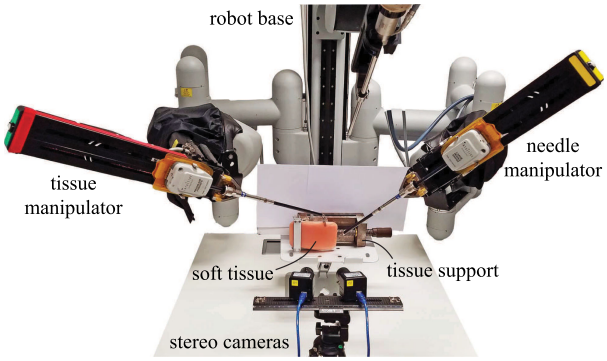

Fig. 10. Experimental set-up for dual-arm robotic needle insertion.

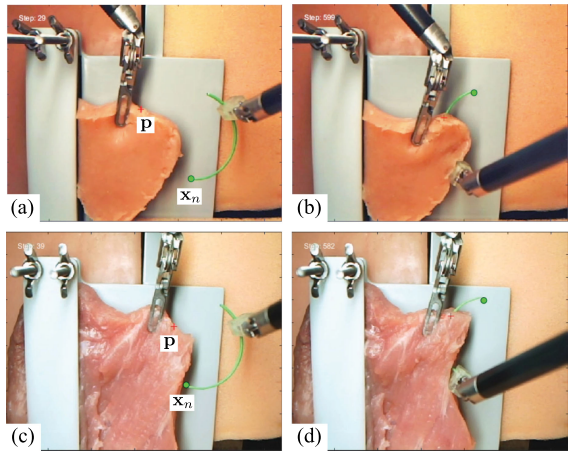

Fig. 11. Needle insertion experiments using phantom tissue (a)–(b) and porcine tissue (c)–(d). The red cross and green dot indicate the target position $\mathbf{p}$ and the (predicted) needle tip position $\mathbf{x}_n$, respectively.

C. Case Study: Minimally-Invasive Suturing

The experiments are carried out using the da Vinci Research Kit (dVRK) as the robot platform (configured as shown in Fig. 10). Two patient-side manipulators are equipped with a Pro-Grasp Forceps (PGF) and a Large Needle Driver (LND) respectively to manipulate the tissue and needle during the procedure. A needle holder is installed on the jaw of the LND to fix the grasping pose of the needle relative to the robot. A 1/2 surgical needle with 17 mm radius is used and painted green for better image segmentation from flesh background. The above configuration aims to simulate the minimally-invasive suturing using surgical robots. The Kanade-Lucas-Tomasi (KLT) optical flow algorithm is implemented using a pair of calibrated stereo cameras to track the pre-selected 3D target position during the procedure. The control algorithm is executed via cisst/SAW libraries and dVRK ROS MATLAB wrapper to communicate between the upper-level controller and the robot actuation.

We use two types of materials for needle insertion, the phantom biological tissue model (synthetic gel, size $\sim$50$\times$50 mm, thickness $\sim$8 mm) and the porcine tissue (size $\sim$100 $\times$ 80 mm, thickness $\sim$10 mm). The tissue is fixed one-side on the table with the other side regulated by robots. The needle is well-observed by at least one camera before stitching such that its pose can be computed as in [33], and is predicted via robot kinematics under occlusion during the insertion. The initial misaligned target error from the needle tip trajectory is set to $\sim$10 mm (random positioned) since the needle placement prior to insertion phase could partially alleviate such error during the suturing task. The update gain for the adaptive estimator is set to $\mathbf{\Gamma} = diag(0.0012, 0.0012, ...) \in \mathbb{R}^{l\times l}$, with the control gain set from $\mathbf{K}$ to be 0.001 for $||\mathbf{p} - \mathbf{x}_n||$ and 0.15 for α. To regulate the motions of the robots, we set the saturated motion speeds for tissue and needle manipulators to be 0.2 mm/s and 0.15 mm/s, respectively. The threshold distance ϵ is set to 1 mm. The final needle insertion error between the target and the needle penetrating point is manually measured in the 3D workspace.

Fig. 11 demonstrates the needle insertion performance using the proposed dual-arm robot control strategy. The asymptotic minimization of the targeting errors for different tissue materials is graphed in Fig. 12(a), with both results reaching errors of $<$1 mm subject to ϵ, compared to a mean 9.6 mm error without

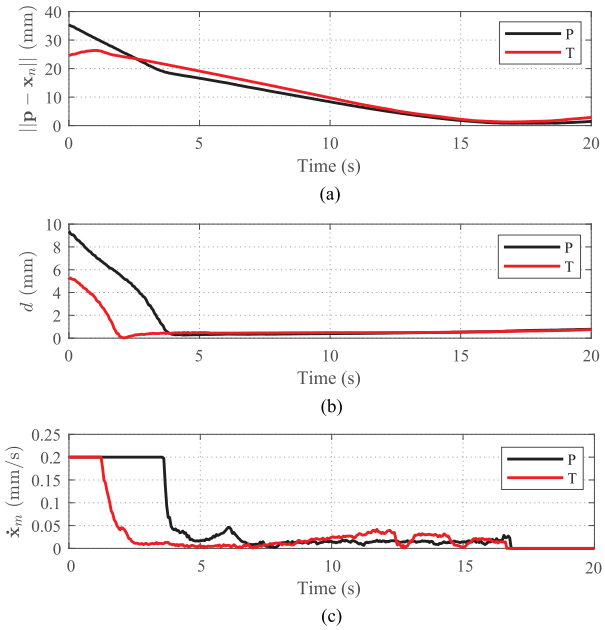

Fig. 12. (a) Evolution of the norm of the tip-target error (P means the case with phantom tissue, T for the one with the porcine tissue. (b) Evolution of the feedback feature d during the insertions. (c) The commanded tissue manipulator velocities during the insertions.

tissue regulation under the identical set-up. The value of feedback feature d descents as time elapses as the needle tends to deviate the target continuously (see Fig. 12(b)). The motion of the tissue manipulator decreases but remains active to regulate the target deviation, as shown in Fig. 12(c). The greater fluctuation of $\dot{\mathbf{x}}_n$ in the case of using porcine tissue results from the tissue heterogeneity which induces estimation uncertainty. The residual insertion error is associated to the inaccuracy in sensor measurement and the estimation result of needle tip position. Results from ten trials reveal a mean minimized error of 0.75 mm (range 0.4$-$0.9 mm, standard deviation 0.28 mm) subject to preset ϵ, compared to the mean 0.9$-$1.3 mm error from manual suturing performed by experienced surgeons reported in [1], [34].

VI. Conclusion

A new dual-arm control strategy integrating active tissue manipulation for robust needle insertion has been presented. We have characterized the tissue deformation behavior by deriving the needle-induced deformation matrix. An adaptive controller has been developed to minimize the needle insertion error by online estimating the deformation properties and camera-robot calibration without knowing their exact knowledge. Both needle and tissue motions are actuated actively via dual-arm coordinated control, with its stability being proved mathematically. Simulations and experiments have been conducted for proof of concept of the proposed algorithm.

Results indicate that our approach can solve the issues of inaccurate initial needle placement and needle-induced target deviation from tissue deformation. Dual-arm control is also proved to be significant to improve target reachability, compared to the open-loop needle insertion in most existing works. The study further shows that the stable control performance is robust to small disturbances, which is important to deal with feedback noise and modelling uncertainties (such as tissue heterogeneity) in real applications. The insertion accuracy is competitive to it from manual execution by human surgeons. The proposed framework is a fundamental step to achieve automated minimally-invasive suturing using dual-arm robots.

One limitation of our work is that the use of kinematic controller could not directly tackle tissue overstretching (possibly causing damage), which usually requires force feedback. However, it could be solved (based on our controller) by means of image-based perception and regulation of tissue deformation. We also assume the target to be constantly trackable during the procedure, which may be difficult in a complex visual environment and should be accompanied by robust image-based tracking algorithm. In the future, we will implement image-based deformation regulation of soft tissue using unstable image features to enhance the reliability of tissue deformation control for autonomous robotic suturing.

References

[1] S. Seki, "Techniques for better suturing," *Brit. J. Surgery*, vol. 75, no. 12, pp. 1181–1184, 1988.

[2] E. E. Deurloo, K. G. Gilhuijs, L. J. S. Kool, and S. H. Muller, "Displacement of breast tissue and needle deviations during stereotactic procedures," *Investigative Radiol.*, vol. 36, no. 6, pp. 347–353, 2001.

[3] R. L. Moy, B. Waldman, and D. W. Hein, "A review of sutures and suturing techniques," *J. Dermatologic Surgery Oncol.*, vol. 18, no. 9, pp. 785–795, 1992.

[4] G. I. Barbash and S. A. Glied, "New technology and health care costs–the case of robot-assisted surgery," *New England J. Med.*, vol. 363, no. 8, pp. 701–704, 2010.

[5] J. Sanchez, J.-A. Corrales, B.-C. Bouzgarrou, and Y. Mezouar, "Robotic manipulation and sensing of deformable objects in domestic and industrial applications: A survey," *Int. J. Robot. Res.*, vol. 37, pp. 688–716, 2018.

[6] S. DiMaio *et al.*, "Robot-assisted needle placement in open MRI: System architecture, integration and validation," *Comput. Aided Surgery*, vol. 12, no. 1, pp. 15–24, 2007.

[7] Y. Yu *et al.*, "Robot-assisted prostate brachytherapy," in *Proc. Int. Conf. Med. Image Comput. Comput. Assist. Intervention*, 2006, pp. 41–49.

[8] R. C. Jackson and M. C. Çavuşoğlu, "Modeling of needle-tissue interaction forces during surgical suturing," in *Proc. IEEE Int. Conf. Robot. Autom.*, 2012, pp. 4675–4680.

[9] D. J. Van Gerwen, J. Dankelman, and J. J. Van den Dobbelsteen, "Needle–tissue interaction forces–a survey of experimental data," *Med. Eng. Phys.*, vol. 34, no. 6, pp. 665–680, 2012.

[10] R. Tsumura, J. S. Kim, H. Iwata, and I. Iordachita, "Preoperative needle insertion path planning for minimizing deflection in multilayered tissues," *IEEE Robot. Autom. Lett.*, vol. 3, no. 3, pp. 2129–2136, Jul. 2018.

[11] E. M. Boctor, M. A. Choti, E. C. Burdette, and R. J. Webster Iii, "Three-dimensional ultrasound-guided robotic needle placement: An experimental evaluation," *Int. J. Med. Robot. Comput.*, vol. 4, no. 2, pp. 180–191, 2008.

[12] G. Zong, Y. Hu, D. Li, and X. Sun, "Visually servoed suturing for robotic microsurgical keratoplasty," in *Proc. IEEE/RSJ Int. Conf. Intell. Robot. Syst.*, 2006, pp. 2358–2363.

[13] P. Hynes, G. I. Dodds, and A. Wilkinson, "Uncalibrated visual-servoing of a dual-arm robot for surgical tasks," in *Proc. Int. Symp. Comput. Intell. Robot. Autom.*, 2005, pp. 151–156.

[14] M. H. Loser and N. Navab, "A new robotic system for visually controlled percutaneous interventions under CT fluoroscopy," in *Proc. Int. Conf. Med. Image Comput. Comput. Assist. Intervention*, 2000, pp. 887–896.

[15] P. Chatelain, A. Krupa, and N. Navab, "3D ultrasound-guided robotic steering of a flexible needle via visual servoing," in *Proc. IEEE Int. Conf. Robot. Autom.*, 2015, pp. 2250–2255.

[16] R. Kojcev *et al.*, "Dual-robot ultrasound-guided needle placement: Closing the planning-imaging-action loop," *Int. J. Comput. Assisted Radiol. Surgery*, vol. 11, no. 6, pp. 1173–1181, 2016.

[17] D. Glozman and M. Shoham, "Image-guided robotic flexible needle steering," *IEEE Trans. Robot.*, vol. 23, no. 3, pp. 459–467, Jun. 2007.

[18] K. B. Reed *et al.*, "Robot-assisted needle steering," *IEEE Robot. Autom. Mag.*, vol. 18, no. 4, pp. 35–46, Dec. 2011.

[19] M. Abayazid, R. J. Roesthuis, R. Reilink, and S. Misra, "Integrating deflection models and image feedback for real-time flexible needle steering," *IEEE Trans. Robot.*, vol. 29, no. 2, pp. 542–553, Apr. 2013.

[20] S. P. DiMaio and S. E. Salcudean, "Needle steering and motion planning in soft tissues," *IEEE Trans. Biomed. Eng.*, vol. 52, no. 6, pp. 965–974, Jun. 2005.

[21] V. Lagerburg, M. A. Moerland, M. van Vulpen, and J. J. Lagendijk, "A new robotic needle insertion method to minimise attendant prostate motion," *Radiotherapy Oncol.*, vol. 80, no. 1, pp. 73–77, 2006.

[22] M. Mahvash and P. E. Dupont, "Fast needle insertion to minimize tissue deformation and damage," in *Proc. IEEE Int. Conf. Robot. Autom.*, 2009, pp. 3097–3102.

[23] R. Alterovitz, K. Y. Goldberg, J. Pouliot, and I.-C. Hsu, "Sensorless motion planning for medical needle insertion in deformable tissues," *IEEE Trans. Inf. Technol. Biomed.*, vol. 13, no. 2, pp. 217–225, Mar. 2009.

[24] Y. Kobayashi *et al.*, "Enhanced targeting in breast tissue using a robotic tissue preloading-based needle insertion system," *IEEE Trans. Robot.*, vol. 28, no. 3, pp. 710–722, Jun. 2012.

[25] M. Torabi, K. Hauser, R. Alterovitz, V. Duindam, and K. Goldberg, "Guiding medical needles using single-point tissue manipulation," in *Proc. IEEE Int. Conf. Robot. Autom.*, 2009, pp. 2705–2710.

[26] V. G. Mallapragada, N. Sarkar, and T. K. Podder, "Robot-assisted real-time tumor manipulation for breast biopsy," *IEEE Trans. Robot.*, vol. 25, no. 2, pp. 316–324, Apr. 2009.

[27] D. Navarro-Alarcon *et al.*, "Automatic 3-D manipulation of soft objects by robotic arms with an adaptive deformation model," *IEEE Trans. Robot.*, vol. 32, no. 2, pp. 429–441, Apr. 2016.

[28] A. C. Barnett, Y.-S. Lee, and J. Z. Moore, "Fracture mechanics model of needle cutting tissue," *J. Manuf. Sci. Eng.*, vol. 138, no. 1, 2016, Art. no. 011005.

[29] A. M. Okamura, C. Simone, and M. D. O'leary, "Force modeling for needle insertion into soft tissue," *IEEE Trans. Biomed. Eng.*, vol. 51, no. 10, pp. 1707–1716, Oct. 2004.

[30] Y.-C. Fung, *Biomechanics: Mechanical Properties of Living Tissues*. Berlin, Germany: Springer, 2013.

[31] A. G. Atkins and Y.-W. Mai, *Elastic and Plastic Fracture: Metals, Polymers, Ceramics, Composites, Biological Materials*. New York, NY, USA: Wiley, 1985.

[32] N. Perez, "Linear-elastic fracture mechanics," in *Fracture Mechanics*. Berlin, Germany: Springer, 2017, pp. 79–130.

[33] F. Zhong *et al.*, "Adaptive 3D pose computation of suturing needle using constraints from static monocular image feedback," in *Proc. IEEE/RSJ Int. Conf. Intell. Robot. Syst.*, 2016, pp. 5521–5526.

[34] S. Seki, "Accuracy of suture techniques of surgeons with different surgical experience," *Japanese J. Surgery*, vol. 17, no. 6, pp. 465–469, 1987.